Available online at www.sciencedirect.com
SCIENCE DIRECT®
International Journal of Heat and Mass Transfer 47 (2004) 5483–5500
International Journal of HEAT and MASS TRANSFER
www.elsevier.com/locate/ijhmt

A mathematical model for atmospheric ice accretion and water flow on a cold surface

T.G. Myers *, J.P.F. Charpin

Department of Mathematics and Applied Mathematics, University of Cape Town, Rondebosch 7701, South Africa

Received 12 January 2004; received in revised form 28 June 2004
Available online 18 September 2004

Abstract

A mathematical model is developed to describe ice accretion and water flow on a cold substrate of arbitrary shape. It is shown how the model may be applied to practical substrate shapes, such as flat surface, cylinder and aerofoil. A numerical scheme to solve the governing equations is then described. Results are presented for an aerofoil under conditions appropriate to in-flight icing and for a cylinder in conditions for atmospheric icing.

Keywords: Aircraft icing; Atmospheric icing; Lubrication theory; Solidification; Thin film flow

1. Introduction

Ice accretion on structures and aircraft is a problem of fundamental importance to a number of industries. Difficulties encountered by the shipping, power transmission and aerospace industries are well documented and the subject of intense current investigation, see [1–4] for example. Power cables and radio masts have been damaged or destroyed on numerous occasions due to the added burden of the ice or an increase in aerodynamic interaction leading to unacceptable movement such as galloping [3,5]. The effort in Canada and the northern US, in particular, has been focussed after the 'Great Ice Storm' of 1998, which caused billions of dollars worth of damage to electrical equipment [3,6]. On aircraft various in-flight incidents have been shown to be directly attributable to ice accretion. This may be due to ice build-up on an aerofoil leading edge, alternatively, ice may build-up on a non-critical surface and subsequently break off, damaging downstream components [7,8]. Similar problems are encountered on the aerofoils of wind turbines. The ice reduces their aerodynamic efficiency and thus decreases power generation. Large accretions may lead to structural failure, see [9]. Ice accretion is also a concern for the shipping industry. Lozowski et al. [4] assert that marine icing is the primogenitor of icing problems, having caused grief for mariners long before aircraft or power cables were even invented.

To predict and therefore combat ice accretion numerous models and codes have been developed. Aircraft icing models and codes are discussed in detail in [1,2]. Models of ice accretion on structures are discussed in [3,5], whilst marine icing is discussed in [4].

Icing models are generally split into two major components. The first component models the air flow and

* Corresponding author. Tel.: +27 21 650 3815; fax: +27 21 650 2334.
E-mail addresses: myers@maths.uct.ac.za (T.G. Myers), jcharpin@maths.uct.ac.za (J.P.F. Charpin).

0017-9310/$ - see front matter © 2004 Elsevier Ltd. All rights reserved.
doi:10.1016/j.ijheatmasstransfer.2004.06.037

Nomenclature

b	ice layer thickness	β	local collection efficiency
c	specific heat	ρ	density
$e(T) \approx e_0 T$	saturation vapour pressure	θ	temperature in water
$\overline{H}$	convective heat transfer coefficient	χ	evaporation/sublimation mass transfer coefficient
h	water layer thickness		
Q	energy source or sink terms		
r	local recovery factor	*Subscripts*	
(s_1, s_2, η)	curvilinear co-ordinate system	a	air
T	temperature in ice	d	droplet
T_α	constant temperature	e	evaporation
W	free stream velocity	i	ice
(x, y, z)	Cartesian co-ordinate system	s	sublimation

droplet trajectories. This provides inputs for the second component which is the actual ice accretion and water flow. Both components have limitations, which is not surprising due to the complexity of predicting flow over a rough accreting surface. In particular the convective heat transfer coefficient is notoriously difficult to measure. The effect of surface roughness on the heat transfer coefficient and current practice in icing codes is discussed in [1]. Another significant limitation of icing codes is the inadequate modelling of film runback and the coupling of the film flow to the accretion [10,11].

The basis of all of the icing components is the simple one-dimensional equilibrium energy balance first described by Messinger [12] (of course writing down the energy balance is simple, obtaining the appropriate parameter values is not). This model also has a number of drawbacks, the most obvious of which is that the temperature in the ice and water layers must always be assumed isothermal so neglecting conduction. This results in a freezing fraction which is always less than the true value [13]. Recently the one-dimensional icing model has been solved by adopting a Stefan approach, namely solving simultaneously for the temperature profiles and layer thicknesses [13,14]. In the limit of a very thin water layer or at large times this model reproduces the accretion rate predicted by Messinger.

In order to accurately predict accretion an icing model must be coupled to a water film flow model. A significant drawback for a number of icing models is that there is little relation between the water flow and the underlying physics. A typical approach is that if a water film exists at a given grid cell at a particular time-step then the unfrozen water moves to the adjacent cell downstream at the next time-step. This means that results are grid size and time-step dependent. However, recently icing models have been developed where the water layer is treated with more care. Poots [5], models it as a steady-state thin film. Bourgault et al. [10] also assume a thin fluid film, in which case lubrication theory may be applied (not shallow water theory as the name of their code implies). This leads to a mass balance involving an unknown film height and accretion rate. Coupling this to a Messinger type energy balance produces a second equation and a third unknown, the equilibrium temperature. Whilst a significant improvement on earlier accretion models this approach still has a number of drawbacks. Firstly, as already discussed, the Messinger approach will underpredict the accretion rate. To overcome this a conduction term is introduced into the energy balance, but there is no way of quantifying this and its use is only discussed when dealing with anti-icing which is not investigated in the paper. Secondly, the water film is driven solely by air shear. Near a stagnation line other forces, such as gravity and surface tension, are required to move the fluid. Neglecting these driving forces will lead to the fluid piling up near the stagnation line and therefore make the model physically unrealistic and numerically unstable. The governing equation for thin film flow driven solely by air shear is hyperbolic and can develop shocks, particularly in the vicinity of a moving contact line [15,16]. Surface tension will prevent these shocks occurring [17]. On structures the ambient pressure is approximately constant (and the air shear may be negligible), on aircraft the pressure changes rapidly and so flow is also driven by pressure gradient. These terms must all be included in the film flow equation. Finally, to reduce the number of unknowns to match the governing equations a number of compatibility relations must be introduced. All of these deficiencies may be overcome by coupling a full film flow model, of the type described in [18], to a Stefan model. This approach has been employed to model the solidification of a fluid on a flat, cold surface in [19]. Myers et al. [16] extend this theory to deal with solidification on an arbitrary substrate.

The main focus of the current paper is to apply the mathematical theory described in [16] to practical situations. Evaporation and sublimation contribute signifi-

cantly to the energy balance but were neglected in the mass balances of [16]. We extend the theory to include these effects into the mass balance and also discuss when it is appropriate to include these terms in structural and aircraft icing models. This has previously been carried out in the context of atmospheric icing in, for example, [5,20]. We start the applications with two simple examples. The simplest reduction is obviously to a flat substrate. We then move onto to an example appropriate to accretion on cables, i.e. a cylindrical substrate. Finally we show the application to an NACA0012 aerofoil. Numerical examples are also given for each case. In particular for the cylinder we consider conditions suitable to structural icing and for the aerofoil for inflight icing conditions. Based on the results we discuss the limits of applicability of the model.

Under certain conditions ice accretions will exhibit sufficiently severe surface roughness for the film to break up and so the roughness elements may be partially dry. In this case the film should be considered as an average quantity over an area encompassing both wet and dry regions. The roughness will play a role by affecting not only the film height but also the ease with which the fluid moves over the surface. This average approach has been successfully applied to water flow over very rough surfaces of partially inundated soil [21]. Poots [5] (and references therein) describes the use of film flow models on accreting ice surfaces and demonstrates the validity of this approach by comparison with experiments. Bourgault et al. [10] have introduced their film flow model into a prototype aircraft icing code. The model developed by Myers et al. [19] deals with ice accretion and water flow on a flat surface. This is currently employed in a commercial aircraft icing code, ICECREMO [1,22].

The original motivation for this work is aircraft icing, however, the models are applicable to ice growth on any cold structure. In particular, ice accretion on a wind turbine occurs in an identical manner to that on aircraft, although the wind speeds are typically lower [3,9,23]. Ice build-up on power lines and related equipment also occurs as a result of in-cloud icing or freezing rain and drizzle [5,3,6]. In a wider context, solidification from a flowing liquid or a droplet spray is of interest in the casting of metals and spray forming, lava flows and hydrate build-up in oil pipelines [24–27].

2. Mathematical model

The model will initially be derived for a flat substrate and then extended to an arbitrary three-dimensional surface. The model configuration is shown in Fig. 1, which is a typical cross-section of an ice and water accretion. The x and y axes define the substrate, the z axis points away from the substrate. Throughout the following work the ice height will be denoted by b, the thickness

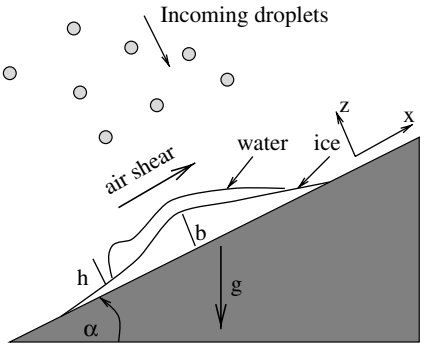

Fig. 1. Model configuration.

of the water layer on top of the ice is h. The temperature in the ice and water is denoted T and θ respectively.

Two main assumptions will be employed in the flow model derivation. The first is that the square of aspect ratio of the flow, ϵ^2, and the reduced Reynolds number, $\epsilon^2 Re$, are both small. This means that the flow can be modelled with lubrication theory. The second is that the effect of temperature on the viscosity, μ_w, and density, ρ_w, of the fluid is relatively small until the sudden change as solidification occurs, therefore, for the flow calculation μ_w and ρ_w are taken as constant. This means that the fluid is incompressible and that the flow effectively decouples from the thermal problem. Hence the mathematical model may be developed in two stages: a flow model and a thermal analysis. The coupling between the fluid flow and thermal models still exists in that the accretion acts as a mass sink for the fluid, whilst the supercooled fluid acts as an energy sink removing heat from the ice layer.

2.1. Fluid flow

Provided ϵ^2 and $\epsilon^2 Re \ll 1$, and the fluid viscosity and density remain constant the Navier–Stokes and continuity equations reduce to

$$\mu_w \frac{\partial^2 u}{\partial z^2} = \frac{\partial p}{\partial x} - \rho_w g \hat{\mathbf{g}} \cdot \hat{\mathbf{x}} + \mathcal{O}(\epsilon^2, \epsilon^2 Re), \tag{1}$$

$$\mu_w \frac{\partial^2 v}{\partial z^2} = \frac{\partial p}{\partial y} - \rho_w g \hat{\mathbf{g}} \cdot \hat{\mathbf{y}} + \mathcal{O}(\epsilon^2, \epsilon^2 Re), \tag{2}$$

$$0 = \frac{\partial p}{\partial z} + \mathcal{O}(\epsilon^2, \epsilon^2 Re), \tag{3}$$

$$\nabla \cdot \mathbf{u} = 0, \tag{4}$$

where $\mathbf{u} = (u, v, w)$ denotes the fluid velocity and p is the fluid pressure. Note, although it is simple to include, gravity is neglected in the z direction since, in general, it is order ϵ smaller than the gravity terms in the x and y directions.

Eqs. (1)–(4) require solving subject to no-slip at the ice–water interface, $z = b$:

$$u = v = \mathcal{O}(\epsilon^2). \tag{5}$$

The no-slip condition is the source of the well-known stress singularity at a moving contact line. This may be overcome in two different ways, either substitute it for a slip condition or specify a precursor film so that the fluid film height never reaches zero. These models are discussed in [18]. In the following, we will impose a precursor film model to both the fluid and ice layers.

Continuity of mass flux provides another condition at $z = b$:

$$\rho_w \mathbf{n}\cdot(\mathbf{u}-\mathbf{u_b}) = \rho_i \mathbf{n}\cdot(\mathbf{u_s}-\mathbf{u_b}), \tag{6}$$

where $\mathbf{u_b} = (0,0,\frac{\partial b}{\partial t})$ is the velocity of the ice accretion surface and $\mathbf{u_s} = \mathbf{0}$ is the velocity of the ice, the normal to the ice surface $\mathbf{n} = \left(-\frac{\partial b}{\partial x}, -\frac{\partial b}{\partial y}, 1\right)$. Expanding Eq. (6) and applying the no-slip condition, Eq. (5), leads to

$$w = \left(1 - \frac{\rho_i}{\rho_w}\right)\frac{\partial b}{\partial t}, \tag{7}$$

where ρ_i and ρ_w are the density of the ice and water respectively. This demonstrates that if $\rho_i = \rho_w$ then $w = 0$ and there is no normal fluid motion at the interface. Normal motion only occurs if there is a mismatch in density between the phases forcing movement to accommodate new ice.

A similar condition to Eq. (6) is imposed at the water–air interface, $z = b + h$. In this case the boundary velocity $\mathbf{u_b} = \left(0,0,\frac{\partial b}{\partial t}+\frac{\partial h}{\partial t}\right)$. The water droplets are assumed to impact vertically with a constant velocity. The appropriate density to replace ρ_i in Eq. (6) is that of the droplet content of the air (liquid water content), ρ_A, where $\rho_A \ll \rho_w$. If evaporation occurs at a rate $\dot{m}_e$ then the appropriate boundary condition is

$$w = \left(1 - \frac{\rho_A}{\rho_w}\right)\left(\frac{\partial b}{\partial t}+\frac{\partial h}{\partial t}\right) + u\left(\frac{\partial b}{\partial x}+\frac{\partial h}{\partial x}\right) + v\left(\frac{\partial b}{\partial y}+\frac{\partial h}{\partial y}\right) - \frac{1}{\rho_w}(\beta \mid \mathbf{W}\cdot\mathbf{n} \mid \rho_A - \dot{m}_e), \tag{8}$$

where the product $\beta|\mathbf{W}\cdot\mathbf{n}|\rho_A$ represents the rate of mass impingement, with catch efficiency β and air velocity $\mathbf{W}$. The evaporation rate will be discussed later. The density of the air/droplet mixture is significantly less than the water density, $\rho_A/\rho_w \ll 1$, and so will be neglected in the first term on the right hand side of (8). The same ratio must be retained in the impingement term since it is multiplied by the air velocity $\mathbf{W}$ which is typically $\mathcal{O}(10^2)\,\mathrm{m\,s^{-1}}$ for an aircraft in flight. Continuity of shear and normal stress at the water–air interface, leads to

$$\mu_w \frac{\partial u}{\partial z} = A_1 + \mathcal{O}(\epsilon^2), \quad \mu_w \frac{\partial v}{\partial z} = A_2 + \mathcal{O}(\epsilon^2), \tag{9}$$

$$p - p_a = -\sigma\nabla^2(b+h) + \mathcal{O}(\epsilon^2), \tag{10}$$

where (A_1, A_2) are the components of shear due to the air flow, they may vary with x, y and t, σ is the surface tension.

A detailed analysis concerning the coupling between the air and water flow is not carried out in the current work, for further information on this subject the reader is referred to Craik [28], King et al. [29], Tsao et al. [30], Yih [31]. Provided the water velocity is significantly less than the free stream velocity, within the current level of approximation it is sufficient to assume the shear stress caused by the air is the same as that which would occur on a dry surface [10,32]. This is termed the primary flow by Yih [31]. The curvature term in Eq. (10), which determines the magnitude of the surface tension induced stress, has been approximated to be consistent with lubrication theory. The total curvature comprises the sum of the curvatures of the ice and water surfaces. This is one way in which the shape of the ice accretion affects the fluid motion. This effect has previously been noted in studies of flow on curved surfaces [16,33,34], where it is termed an 'overpressure'. In the following section it is shown how the substrate shape enters into the pressure equation.

The fluid pressure may be determined immediately by integrating Eq. (3) subject to the boundary condition, Eq. (10):

$$p - p_a = -\sigma\nabla^2(b+h). \tag{11}$$

Integrating Eqs. (1) and (2) subject to Eqs. (5) and (9) gives the fluid velocities:

$$\mu_w u = \frac{1}{2}\left(\frac{\partial p}{\partial x} - \rho_w g\hat{\mathbf{g}}\cdot\hat{\mathbf{x}}\right)(z^2 - b^2 - 2(z-b)(b+h)) + A_1(z-b), \tag{12}$$

$$\mu_w v = \frac{1}{2}\left(\frac{\partial p}{\partial y} - \rho_w g\hat{\mathbf{g}}\cdot\hat{\mathbf{y}}\right)(z^2 - b^2 - 2(z-b)(b+h)) + A_2(z-b). \tag{13}$$

Integrating the continuity equation (4) across the film gives

$$w|_{b+h} - w|_b = -\int_b^{b+h}\left(\frac{\partial u}{\partial x}+\frac{\partial v}{\partial y}\right)\mathrm{d}z. \tag{14}$$

Applying Leibniz' theorem and substituting for w via Eqs. (7) and (8) leads to the mass balance

$$\rho_w\left(\frac{\partial h}{\partial t} + \nabla\cdot\mathbf{Q}\right) = \beta \mid \mathbf{W}\cdot\mathbf{n} \mid \rho_A - \dot{m}_e - \rho_i\frac{\partial b}{\partial t}, \tag{15}$$

where the fluid flux

$$\mathbf{Q} = \left(-\frac{h^3}{3\mu_w}\left(\frac{\partial p}{\partial x} + G_1\right) + \frac{h^2}{2\mu_w}A_1, -\frac{h^3}{3\mu_w}\left(\frac{\partial p}{\partial y} + G_2\right) + \frac{h^2}{2\mu_w}A_2\right), \tag{16}$$

and $(G_1, G_2) = \rho_w g(\hat{\mathbf{g}} \cdot \hat{\mathbf{x}}, \hat{\mathbf{g}} \cdot \hat{\mathbf{y}})$. The evaporation term may be estimated by considering an energy balance, this is discussed in the following section.

Eq. (15) is a fourth-order nonlinear degenerate partial differential equation, typical of free surface flows involving surface tension. A review of similar equations may be found in Myers [18]. For structural icing gravity is typically the dominant force away from the contact line. In aircraft icing the air shear will dominate, except in the vicinity of the stagnation line where gravity and surface tension will drive the flow. The ambient pressure, p_a will also vary rapidly around the aerofoil, hence pressure gradient plays an important role in driving the flow. In the work of Bourgault et al. [10] air shear is taken as the sole driving force, i.e. the flux is determined by (16) with $p_x = p_y = G_i = 0$. There is therefore no physical mechanism for moving fluid away from the stagnation line.

2.2. Modification for curved surfaces

Eq. (15) is appropriate for flow on a substrate where the curvature is significantly less than the film thickness. This limitation may be partially overcome by approximating the surface with a series of flat plates and then matching over each plate. However, this will never accurately reflect the pressure driving force which is dependent on the surface curvature. This is particularly important when modelling flow near corners or over cylindrical surfaces such as cables or pitot tubes. To accurately model flow on an arbitrary three-dimensional curved surface equation (15) must be modified to

$$\frac{\partial h}{\partial t} + \nabla_s \cdot \mathbf{Q} = \frac{\rho_A}{\rho_w}\beta \mid \mathbf{W} \cdot \mathbf{n} \mid - \frac{1}{\rho_w}\dot{m}_e - \frac{\rho_i}{\rho_w}\frac{\partial b}{\partial t}. \tag{17}$$

In this case the surface is represented by

$$\mathbf{r} = (x, y, z) = \mathbf{R}(s_1(x, y, z), s_2(x, y, z)),$$

where (s_1, s_2) are surface co-ordinates in the principal directions. (Note, both surface co-ordinates must be lengths, so for example, in the case of icing on a cylinder one obvious co-ordinate would be the angle θ however the correct system would be in terms of arc-length $R\theta$). The co-ordinate perpendicular to the plane is η. A typical configuration is shown on Fig. 2. The standard first and second fundamental forms are [35]

$$E = \frac{\partial \mathbf{R}}{\partial s_1} \cdot \frac{\partial \mathbf{R}}{\partial s_1}, \quad G = \frac{\partial \mathbf{R}}{\partial s_2} \cdot \frac{\partial \mathbf{R}}{\partial s_2}, \tag{18}$$

$$L = \frac{\partial^2 \mathbf{R}}{\partial s_1^2} \cdot \mathbf{n}, \quad N = \frac{\partial^2 \mathbf{R}}{\partial s_2^2} \cdot \mathbf{n} \tag{19}$$

and the outward unit normal is

$$\mathbf{n} = \frac{1}{(EG)^{1/2}} \frac{\partial \mathbf{R}}{\partial s_1} \wedge \frac{\partial \mathbf{R}}{\partial s_2}. \tag{20}$$

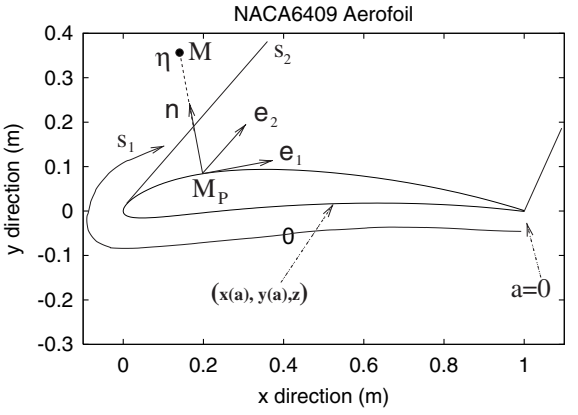

Fig. 2. Co-ordinate system for an arbitrary substrate.

The surface divergence operator in Eq. (17) may now be defined

$$\nabla_s \cdot \mathbf{Q} = \frac{1}{(EG)^{1/2}}\left(G^{1/2}\frac{\partial}{\partial s_1}Q^{s_1} + E^{1/2}\frac{\partial}{\partial s_2}Q^{s_2}\right). \tag{21}$$

The flux components in the principal directions are

$$Q^{s_1} = -\frac{h^3}{3\mu_w}\left(\frac{1}{E^{1/2}}\frac{\partial p}{\partial s_1} + G_1\right) + A_1\frac{h^2}{2\mu_w}, \tag{22}$$

$$Q^{s_2} = -\frac{h^3}{3\mu_w}\left(\frac{1}{G^{1/2}}\frac{\partial p}{\partial s_2} + G_2\right) + A_2\frac{h^2}{2\mu_w}. \tag{23}$$

In this case $(G_1, G_2) = \rho_w g(\mathbf{g}\cdot\mathbf{e_1}, \mathbf{g}\cdot\mathbf{e_2})$. The unit vectors in the s_1 and s_2 directions are

$$\mathbf{e}_1 = \frac{1}{E^{1/2}}\frac{\partial \mathbf{R}}{\partial s_1}, \quad \mathbf{e}_2 = \frac{1}{G^{1/2}}\frac{\partial \mathbf{R}}{\partial s_2}. \tag{24}$$

The fluid pressure is

$$p = p_0 - \sigma\left(\kappa_1 + \kappa_2 + (b+h)(\kappa_1^2 + \kappa_2^2) + \frac{1}{E}\frac{\partial^2}{\partial s_1^2}(b+h) + \frac{1}{G}\frac{\partial^2}{\partial s_2^2}(b+h)\right). \tag{25}$$

The substrate curvatures are defined as

$$\kappa_1 = \frac{L}{E}, \quad \kappa_2 = \frac{N}{G}. \tag{26}$$

It is worth comparing this expression with the pressure derived on a flat surface. Eq. (11) depends on surface tension through the term $\nabla^2(b+h)$. This indicates that surface tension only acts to drive the fluid through the variation of the position of the top surface of the fluid. In Eq. (25) there are extra terms due to the surface curvature. These can have a strong effect on the flow when the curvature is high. A familiar example is encountered in the painting of corners. At convex corners the fluid drains away leaving a relatively thin coating. At concave corners the opposite happens and fluid

is drawn in. Further details may be found in Myers et al. [16].

The application of Eq. (17) for practical situations will be demonstrated in coming sections. However the mass sink terms, reflecting the evaporation and ice accretion, which appear as the final terms on the right hand side of both (15) and (17) must first be determined. This is done by considering the thermal problem.

2.3. Thermal problem

Before solving the flow equation an expression for the freezing rate, $\partial b/\partial t$, is required. This is determined by considering the thermal problem, which is governed by heat equations in the ice and water layers. Note, we do not consider spongy ice, which is postulated to be isothermal [3], but this is an obvious extension to the model.

The limit of particular interest to the present study is when the ice and water layers are sufficiently thin that conduction is the dominant method of heat transfer. For an accreting ice surface this will hold provided the ice layer is less than 2.4 cm and the water layer less than 3 mm [13,14]. In this situation, terms of $\mathcal{O}(Pe)$, where the Peclet number, Pe, is the ratio of advection to conduction terms, will therefore be neglected; this will be discussed later. To be consistent with the previous section, terms of $\mathcal{O}(\epsilon^2)$ will also be neglected. The heat equations then reduce to pseudo-steady forms:

$$\frac{\partial^2 T}{\partial \eta^2} = \mathcal{O}(\epsilon^2, Pe), \tag{27}$$

$$\frac{\partial^2 \theta}{\partial \eta^2} = \mathcal{O}(\epsilon^2, Pe), \tag{28}$$

where T and θ are the ice and water temperatures respectively. On a flat substrate the appropriate equations are obtained by substituting z for η. Eqs. (27) and (28) are solved subject to the following conditions.

- At the substrate, $\eta = 0$, the ice is in perfect thermal contact with the substrate, which has high conductivity and a thermal mass much greater than that of the ice accretion.

  $$T = T_s, \tag{29}$$

  where T_s is the substrate temperature. This will typically be the same as the ambient temperature but will be left in this form to keep the model general. This condition is particularly relevant to aircraft, where ice forms on only a relatively small portion of the wing. Since this is typically metal any excess heat generated will quickly be conducted away and the wing temperature will remain relatively constant.

The remaining boundary conditions depend on whether rime or glaze ice grows.

- When rime ice grows, the ice surface $\eta = b$ is cooled according to

  $$\frac{\partial T}{\partial \eta} = \frac{Q_l + Q_k + Q_a - Q_d - Q_h - Q_s}{\kappa_i} = E_r - F_r T. \tag{30}$$

  Typical values for these terms may be found in Table 1.
- When glaze ice grows, the ice–water interface $\eta = b$ is at the freezing temperature

  $$T = \theta = T_f. \tag{31}$$

- The air–water interface, $\eta = b + h$, is subject to

  $$\frac{\partial \theta}{\partial \eta} = \frac{Q_k + Q_a - Q_d - Q_h - Q_e}{\kappa_w} = E_g - F_g \theta, \tag{32}$$

  The terms E_r, F_r, E_g, F_g have been introduced to simplify the notation.

$$E_r = \frac{Q_l + Q_k + Q_a + q_d T_d + (q_h + q_s) T_a}{\kappa_i},$$

$$F_r = \frac{q_d + q_h + q_s}{\kappa_i},$$

$$E_g = \frac{Q_k + Q_a + q_d T_d + (q_h + q_e) T_a}{\kappa_w},$$

$$F_g = \frac{q_d + q_h + q_e}{\kappa_w}.$$

They depend on the energy source and sink terms. The energy source terms are the droplet kinetic energy and aerodynamic heating [5,2]

$$Q_k = \frac{\rho_A \beta W^3}{2}, \quad Q_a = \frac{r \overline{H} W^2}{2 c_a}$$

and, in the case of rime ice growth, the release of latent heat $Q_l = L_f \beta |\mathbf{W}\cdot\mathbf{n}| \rho_A$. The energy sink terms are cooling by the incoming droplets, convective heat transfer, radiative heat flux and evaporation

$$Q_d = \rho_A \beta \mid \mathbf{W}\cdot\mathbf{n} \mid c_w(\theta - T_d) = q_d(\theta - T_d),$$

$$Q_h = \overline{H}(\theta - T_A) = q_h(\theta - T_A),$$

$$Q_r = \epsilon \sigma_r(\theta^4 - T_A^4) \approx 4\epsilon\sigma_r T_A^3(\theta - T_A) = q_r(\theta - T_A),$$

Table 1
Energy terms

Q_a	1747	Q_k	182	Q_l	15048
q_d	18.9	q_e	423	q_h	500
q_s	517				
E_r	1.351×10^5	F_r	475		
E_g	4.455×10^5	F_g	1.43×10^3		

$$Q_e = \chi_e(e(\theta) - e(T_A)) \approx \chi_e e_0(\theta - T_A) = q_e(\theta - T_A).$$

Both the radiative heat flux and evaporation terms may be approximated by linear expressions [5,13]. For rime ice growth evaporation is replaced by sublimation

$$Q_s = \chi_s(e(T) - e(T_A)) \approx \chi_s e_0(T - T_A) = q_s(\theta - T_A).$$

Further details on the energy terms appropriate to atmospheric icing may be found in [2–5].

Perhaps the most controversial aspect of the above boundary conditions is the calculation of the heat transfer coefficient. Bourgault et al. [10] use a compressible Navier–Stokes solver to determine the outer flow solution which automatically produces heat transfer coefficients. Methods currently employed in commercial codes to determine heat transfer in laminar and turbulent flows on both smooth and rough surfaces and empirical models are discussed in [2,1]. Other methods to estimate this quantity may be found in Poots [5](p.74), Makkonen [3,36] and Arnold et al. [37].

2.3.1. Rime ice growth

If no water layer is present, then rime ice forms and the mass balances of Eqs. (15) or (17) reduce to

$$\frac{\partial b}{\partial t} = \frac{1}{\rho_i}(\beta \mid \mathbf{W}\cdot\mathbf{n} \mid \rho_A - \dot{m}_s). \tag{33}$$

The density of rime ice can vary by a significant amount depending upon the ambient conditions, it may also vary with time for a given ice accretion in which case $\rho_i = \rho_i(t)$. The flow around an accreting ice surface will also be time dependent, in which case β and $|\mathbf{W}\cdot\mathbf{n}|$ will vary. Time dependent terms on the right hand side of Eq. (33) mean that it must be integrated numerically. Although it is clearly a simple matter to numerically integrate a linear first-order equation, in the following examples we will consider the simplest case where all of these quantities remain constant. In particular, the ice density is taken as an average between typical rime and glaze values, $\rho_i = (917 + 880)/2 \approx 898\,\mathrm{kg\,m^{-3}}$ (note Makkonen et al. [9] take $\rho_i = 890$). We will also use this value for glaze accretions. Obviously, for more accuracy, ρ_i could be replaced by a true rime value, which may be significantly lower than 880 and possibly time dependent, in (33) and in the following glaze ice section by an appropriate glaze ice value.

With constant values on the right hand side Eq. (33) may be integrated analytically

$$b = \frac{1}{\rho_i}(\beta \mid \mathbf{W}\cdot\mathbf{n} \mid \rho_a - \dot{m}_s)t. \tag{34}$$

Except for regions of very low catch the sublimation mass loss $\dot{m}_s$ is significantly less than the catch in Eq. (33). This is easily demonstrated by considering the sublimation energy term, Q_s. This energy must equal the rate of mass loss multiplied by the latent heat of sublimation

$$L_s\dot{m}_s = \chi_s e_0(T - T_A).$$

Typical values for the various constants are given in Table 2. For a temperature drop of 5 °C between the ice surface and the air this shows $\dot{m}_s \approx 9.1 \times 10^{-4}\,\mathrm{m\,s^{-1}}$. On an aircraft $W = \mathcal{O}(10^2)\cdot\mathrm{s^{-1}}$ and $\rho_a = 10^{-3}\,\mathrm{kg\,m^{-3}}$. The impinging mass rate, is therefore typically an order of magnitude greater than the sublimation rate and so for aircraft icing sublimation may be neglected (in the mass balance, but not the energy balance) except in regions of very low catch. The slower free stream velocities encountered in structural icing means that sublimation or evaporation may be important in the mass balance. To keep the model as general as possible the mass loss rate $\dot{m}_s$ will be retained in Eq. (33).

The temperature profile follows from Eq. (27) subject to (29) and (30)

$$T = T_s + \frac{E_r - F_r T_s}{1 + F_r b}\eta. \tag{35}$$

Comparing the components of E_r and F_r given in Table 1, it is clear that the coefficient of η on the right hand side of (35) is positive, unless the substrate is significantly hotter than the air temperature. Provided the

Table 2
Parameter values used for Figs. 2–5

c_a	1014	$\mathrm{J\,kg^{-1}\,K^{-1}}$	L_E	2.5×10^6	$\mathrm{J\,kg^{-1}}$
c_w	4220	$\mathrm{J\,kg^{-1}\,K^{-1}}$	W	90	$\mathrm{m\,s^{-1}}$
e_0	44.4	$\mathrm{Pa\,K^{-1}}$	β	0.5	
l_e	0.875		κ_i	2.18	$\mathrm{W\,m^{-1}\,K^{-1}}$
p_0	9×10^4	Pa	κ_w	0.571	$\mathrm{W\,m^{-1}\,K^{-1}}$
r	0.895		ρ_a	0.001	$\mathrm{kg\,m^{-3}}$
$\overline{H}_{aw}$	500	$\mathrm{W\,m^{-2}\,K^{-1}}$	ρ_i	898	$\mathrm{kg\,m^{-3}}$
$\overline{H}_{is}$	1000	$\mathrm{W\,m^{-2}\,K^{-1}}$	ρ_s	2710	$\mathrm{kg\,m^{-3}}$
$\overline{H}_{as}$	1000	$\mathrm{W\,m^{-2}\,K^{-1}}$	ρ_w	1000	$\mathrm{kg\,m^{-3}}$
L_f	3.344×10^5	$\mathrm{J\,kg^{-1}}$	χ_e	9.53	$\mathrm{m\,s^{-1}}$
L_s	2.83×10^6	$\mathrm{J\,kg^{-1}}$	χ_s	11.65	$\mathrm{m\,s^{-1}}$

substrate is not heated, Eq. (35) indicates that the temperature increases away from the substrate, since the heating terms (latent heat in particular) are stronger than the cooling terms.

These expressions for ice thickness and temperature completely solve the problem for rime-ice growth. The ice thickness is determined by the mass balance (33). It may be solved numerically if the input parameters vary with time. If the inputs are constant (for example with a one-step calculation) then Eq. (34) gives an exact expression for the ice thickness for all time. For rime ice growth the ice thickness depends entirely on the incoming fluid and to a lesser extent the sublimation. However, it is important to solve the thermal problem since this determines when, or if, water appears and therefore when to switch to a glaze ice model.

2.3.2. Glaze ice growth

When water appears on the ice layer the leading order temperature in the ice and water satisfy the quasi-steady equations (27) and (28), which require solving subject to 29,31,32. The temperature profiles are given by

$$T = T_s + (T_f - T_s)\frac{\eta}{b}, \tag{36}$$

$$\theta = T_f + \frac{E_g - F_g T_f}{1 + F_g h}(\eta - b). \tag{37}$$

For glaze ice growth the thermal problem is coupled to the fluid flow through the water layer thickness, h, in (37) and the ice accretion rate and thickness which appear in (15). Consistent with the level of approximation applied in previous sections the energy balance is a standard Stefan condition:

$$\rho_i L_f \frac{\partial b}{\partial t} = k_i \frac{\partial T}{\partial z} - k_w \frac{\partial \theta}{\partial z} + \mathcal{O}(\epsilon^2). \tag{38}$$

The temperature gradients may be determined from (37) and (36), substituting these into (38) provides the governing equation for the ice accretion

$$\rho_i L_f \frac{\partial b}{\partial t} = k_i \frac{T_f - T_s}{b} - k_w \frac{E_g - F_g T_f}{1 + F_g h}. \tag{39}$$

The glaze problem is now reduced to its final form. This involves the solution of the coupled mass and energy balances (15) and (39), which must be solved for the ice and water layer thicknesses, b and h. Once this is achieved the temperature in each layer is determined via (36) and (37). Note, the form of energy balance (39) does not preclude time variation in the model inputs, such as the energy terms, E_g and F_g.

The model that is most related to the present one in the literature (to the authors knowledge) is that of Bourgault et al. [10]. As previously stated, their mass balance has air shear as the only driving force. Their energy balance, with the current notation, takes the form

$$\rho_w \left[\frac{\partial}{\partial t}(hc_w\overline{T}) + \nabla\cdot(\bar{u}hc_w\overline{T})\right] = Q_d + Q_k - \frac{1}{2}(Q_e + Q_s) + Q_l + Q_h - \rho_i c_i \overline{T}\frac{\partial b}{\partial t} + \sigma_R(T_\infty^4 - \overline{T}^4) + Q_{cond}, \tag{40}$$

where $\bar{u}$ is the average fluid velocity, σ_R is the Stefan–Boltzmann constant and Q_{cond} represents conduction through the ice. There are three unknowns in (40), namely the ice (or ice growth rate) and water heights and the 'equilibrium temperature' in the air/water/ice/substrate, $\overline{T}$. The mass and energy balances only provide two equations. This problem is circumvented by the introduction of various compatibility relations. However, it is clear from the physics of the problem that the ice growth rate and temperature must be related and this is shown in the current analysis. Further insight from the current work shows that since the water layer is thin, water flow is not a dominant method of heat transfer and, within the level of approximations made to derive the mass balance, the terms on the left hand side of (40) are negligible. Radiative heat transfer in general is negligible since most icing events occur under cloud cover. Eq. (40) may therefore be reduced to

$$\rho_i(L_f - c_i\overline{T})\frac{\partial b}{\partial t} = \frac{1}{2}(Q_e + Q_s) - (Q_d + Q_h + Q_k + Q_{cond}). \tag{41}$$

The present energy balance may be written as

$$\rho_i L_f \frac{\partial b}{\partial t} = Q_e + Q_d + Q_h - (Q_a + Q_k) + \kappa_i \frac{T_f - T_s}{b}. \tag{42}$$

This further highlights the differences in the models. (Note, the difference in signs for Q_d and Q_h is due to their use of a reference temperature and does not indicate a discrepancy.) Since this is a glaze model there is no sublimation, so Q_s should not be included in (41). The final term on the right hand side of (42) is an explicit representation of the conduction term. However, since the temperature is constant throughout the ice and water in (41) this cannot be represented by Q_{cond}. Finally, the ice forms at the interface where the temperature is the freezing temperature, T_f, and the latent heat release is exactly $L_f\dot{b}$. This term balances with the energy terms on the right hand side. These energy terms depend on the surrounding temperatures. In particular the water temperature relates to the evaporation rate and convective cooling. In the current model the water temperature is determined as part of the solution, whereas in Eq. (41) the water temperature is unknown and in fact is averaged as stated above. Since the energy terms on the right hand side of (41) do not contain the correct temperature a correction term must be included. This is the purpose of $c_i\overline{T}$.

In its present form the mathematical description of glaze ice growth is complex, requiring the solution of

coupled fourth- and first-order nonlinear partial differential equations. In particular, the mass balance (15), in the absence of ice formation, is typical of free surface thin film flows. These are notoriously difficult to solve in the vicinity of a moving contact line [38,39,18,40]. For this reason the numerical work of the following sections deals initially with the water flow; the complication of freezing is a relatively simple extension. However, before solving the full problem, the one-dimensional problem and various limiting cases will be considered, to provide a clearer understanding of the model.

3. One-dimensional problem

Whilst unrealistic when water is flowing the one-dimensional model does provide realistic solutions during the rime stage and must be considered to determine when the transition from rime to glaze occurs.

In one-dimension the problem is governed by the mass balance

$$\rho_w \frac{\partial h}{\partial t} = \rho_A \beta \mid \mathbf{W}\cdot\mathbf{n} \mid - \rho_i \frac{\partial b}{\partial t} - \dot{m}_s \tag{43}$$

and the energy balance (39). Poots [5] studies a simplified version of (39), which neglects heat conduction through the water layer, so the energy term $F_g h \equiv 0$ and the ice layer thickness is independent of the water layer thickness. This form of (39) may be integrated immediately. In two and three dimensions, when the driven water film is thin, $F_g h \ll 1$, this is a reasonable assumption. However, in one dimension $F_g h$ is typically $\mathcal{O}(1)$ and should be retained. This is demonstrated in [14].

The assumption that $T(0,t) = T_s < T_f$ means that there will always be a period (possibly very short) when all of the incoming fluid turns to rime ice. This is due to the fact that the initial impacting fluid will almost immediately adopt the substrate temperature. Since this is below freezing and there is a nucleation site, the fluid must freeze. Subsequently, water may appear and glaze ice forms.

Detailed examination of the early stages of ice accretion on aircraft may show water flowing before ice appears. This typically occurs when the air temperature is relatively high, in which case, air compressibility can lead to above freezing temperatures in the vicinity of the wing. Ice accretion only occurs subsequently, when evaporation of the surface water has cooled the substrate below freezing.

Provided the parameter values are independent of time, initially, the ice thickness is given by (34). When water appears the integrated form of Eq. (43) gives an expression for the water height in terms of the unknown ice thickness:

$$h = \frac{\rho_A}{\rho_w}\beta \mid \mathbf{W}\cdot\mathbf{n} \mid (t - t_w) - \frac{\rho_i}{\rho_w}(b - b_w), \tag{44}$$

where b_w and t_w are the ice thickness and time at which water first appears. To determine the ice thickness, Eq. (44) may be used to replace h in (39), giving an equation with a single unknown, b. This must be integrated numerically. Once the ice thickness is known the water thickness and the temperatures in the ice and water can be determined from (44),(36) and (37).

Water first appears when the rime ice temperature reaches the freezing temperature. This is determined from (35), leading to the required expressions for b_w and t_w:

$$b_w = \frac{T_f - T_s}{E_r - F_r T_s}, \quad t_w = \frac{\rho_i b_w + \dot{m}_s}{\rho_A \beta \mid \mathbf{W}\cdot\mathbf{n} \mid}. \tag{45}$$

This is an exact formula, in terms of the input parameters, to determine when glaze ice starts to form. If the denominator, $E_r - F_r T_s \leqslant 0$ Eq. (45) indicates water will never appear and the accretion will be pure rime ice. Rearranging this expression gives the appropriate ambient temperature for pure rime ice growth

$$T_a \leqslant T_f(q_d + q_h + q_s) - (Q_l + Q_k + Q_a). \tag{46}$$

For the parameter values given in Table 2 (relevant to aircraft icing) this condition indicates a value of $T_a = 256.6\,\mathrm{K} = -16.6\,^\circ\mathrm{C}$. This and the formula for transition thickness (45) have been to shown to agree well with experimental observations, see [13,14].

In [13] the current one-dimensional model is compared with the standard Messinger model [12]. It is shown that the current one-dimensional theory leads to physically sensible results with a smooth decrease in the freezing fraction (the ratio of mass freezing to that entering the system) from the rime value of unity to a constant large time value. The Messinger model predicts a discontinuity as the freezing fraction jumps from unity to another, constant lower value. This value is in fact the large time solution of the current model. It was subsequently shown that the Messinger model underpredicts the ice growth rate and the difference between the current and Messinger model grows as the temperature increases.

4. Standard forms

In this section we demonstrate how the flow equation may be applied to the three obvious practical substrate shapes, namely flat, aerofoil and cylindrical. The flat substrate is modelled first, since this is the simplest example and therefore demonstrates the method most clearly. Subsequently an aerofoil shape is described and then the reduction to a cylinder briefly discussed. The energy balance, to determine the ice thickness, is

not shape dependent and so remains the same for all models.

4.1. Reduction to the flat surface model

When the substrate is flat it may be defined as a surface with $z = 0$. The substrate may then be described in terms of the two surface co-ordinates $s_1 = x$, $s_2 = y$. The substrate is defined in terms of these two co-ordinates, $\mathbf{R} = (x, y, 0)$. Obviously the normal co-ordinate $\eta = z$. The first and second fundamental forms are given by Eqs. (18) and (19)

$$E = \frac{\partial \mathbf{R}}{\partial x} \cdot \frac{\partial \mathbf{R}}{\partial x} = 1, \quad G = \frac{\partial \mathbf{R}}{\partial y} \cdot \frac{\partial \mathbf{R}}{\partial y} = 1,$$

$$L = \mathbf{n} \cdot \frac{\partial^2 \mathbf{R}}{\partial x^2} = 0, \quad N = \mathbf{n} \cdot \frac{\partial^2 \mathbf{R}}{\partial y^2} = 0.$$

The substrate and normal vectors are given by Eqs. (24) and (20)

$$\mathbf{e}_1 = \frac{1}{E^{1/2}} \frac{\partial \mathbf{R}}{\partial x} = (1, 0, 0), \quad \mathbf{e}_2 = \frac{1}{G^{1/2}} \frac{\partial \mathbf{R}}{\partial y} = (0, 1, 0),$$

$$\mathbf{n} = \mathbf{e}_1 \wedge \mathbf{e}_2 = (0, 0, 1).$$

This definition of the fundamental forms and co-ordinate system allows the appropriate flow description to be calculated. Firstly, the substrate curvatures, defined by Eq. (26), are zero: $\kappa_1 = L/E = 0$, $\kappa_2 = N/G = 0$. The fluid pressure is then given by Eq.(25). The flow is governed by Eq. (17) where the surface operator ∇_s is the standard divergence, given by Eq. (21). Finally, the fluxes are given by (22) and (23).

4.2. Reduction to a cylinder

If the substrate is a circular cylinder of radius R then it may be parametrised in cylindrical polar coordinates by setting $s_1 = R\theta$, $s_2 = z$ (note, the surface co-ordinates must be lengths), so that the substrate is defined by $\mathbf{R} = (R\cos\theta, R\sin\theta, z)$. The first and second fundamental forms, according to (18) and (19) are

$$\begin{aligned} E &= \frac{\partial \mathbf{R}}{\partial s_1} \cdot \frac{\partial \mathbf{R}}{\partial s_1} = \frac{1}{R^2} \frac{\partial \mathbf{R}}{\partial \theta} \cdot \frac{\partial \mathbf{R}}{\partial \theta} = 1, \\ G &= \frac{\partial \mathbf{R}}{\partial s_2} \cdot \frac{\partial \mathbf{R}}{\partial s_2} = \frac{\partial \mathbf{R}}{\partial z} \cdot \frac{\partial \mathbf{R}}{\partial z} = 1, \end{aligned} \tag{47}$$

$$L = \frac{1}{R^2} \frac{\partial^2 \mathbf{R}}{\partial \theta^2} \cdot \mathbf{n} = \pm \frac{1}{R}, \quad N = \frac{\partial^2 \mathbf{R}}{\partial z^2} \cdot \mathbf{n} = 0. \tag{48}$$

The substrate is defined by the vectors (24)

$$\begin{aligned} \mathbf{e_1} &= \frac{1}{E^{1/2}} \frac{\partial \mathbf{R}}{\partial s_1} = (-\sin\theta, \cos\theta, 0), \\ \mathbf{e_2} &= \frac{1}{G^{1/2}} \frac{\partial \mathbf{R}}{\partial s_2} = (0, 0, 1), \end{aligned} \tag{49}$$

$$\mathbf{n} = \pm \mathbf{e_1} \times \mathbf{e_2}. \tag{50}$$

For flow on the outside of a cylinder the outward normal is $\mathbf{n} = (\cos\theta, \sin\theta, 0)$, flow on the inside requires $\mathbf{n} = -(\cos\theta, \sin\theta, 0)$.

The curvature terms, defined by (26), are then $\kappa_1 = \pm 1/R$, $\kappa_2 = 0$, where $\kappa_1 > 0$ denotes flow inside a cylinder, $\kappa_1 < 0$ denotes flow on the outside. The governing equations then follow in the same way as above, i.e. the pressure is given by (25). The flow is governed by Eq. (17), the surface operator ∇_s by Eq. (21) and the fluxes by (22) and (23).

Note these results may be retrieved from the following case using $x_0(a) = R\cos(a)$ and $y_0(a) = \pm R\sin(a)$. Both circular cylinder and flat substrate models have been studied previously in [16,19].

4.3. Reduction to an aerofoil

In general an arbitrary substrate may be described in terms of two dummy parameters a_1, a_2, so that $\mathbf{R} = [x_0(a_1, a_2), y_0(a_1, a_2), z_0(a_1, a_2)]$. To use this description on an aerofoil we must specify appropriate functions x_0, y_0 and z_0. In the following derivation, to avoid complication, we will investigate an aerofoil of constant cross-section (i.e. no z variation) so $\mathbf{R} = [x_0(a_1), y_0(a_1), z_0(a_2) = a_2]$. This configuration is shown in Fig. 2. To reduce the number of subscripts a_1 will now be denoted a and a_2 by z. The value $a = 0$ corresponds to the tail of the aerofoil, as shown in Fig. 2, by increasing a we move in a clockwise manner. The curvilinear coordinate may then be calculated

$$s_1 = \int_0^a \sqrt{x_0'(t)^2 + y_0'(t)^2}\, \mathrm{d}t + C, \tag{51}$$

where C is a constant such as $s_1 = 0$ corresponds to the leading edge. Positive and negative values for s_1 then correspond to the upper and lower part of the aerofoil respectively. As the substrate has a constant section, the second curvilinear coordinate is $s_2 = z$. The normal coordinate, η, is defined using the normal projection of the considered point (X, Y, Z) onto the substrate:

$$\eta = \overrightarrow{M_P M} \cdot \mathbf{n} = \frac{[Y - y_0(a_p)]x_0'(a_p) - [X - x_0(a_p)]y_0'(a_p)}{\sqrt{x_0'(a_p)^2 + y_0'(a_p)^2}} \tag{52}$$

and a_p satisfies:

$$\begin{aligned} \overrightarrow{M_P M} \wedge \mathbf{n} = \mathbf{0} \Longleftrightarrow\ & [X - x_0(a_p)]x_0'(a_p) \\ & + [Y - y_0(a_p)]y_0'(a_p) = 0. \end{aligned} \tag{53}$$

The first and second fundamental forms are therefore:

$$E = \frac{\partial \mathbf{R}}{\partial s_1} \cdot \frac{\partial \mathbf{R}}{\partial s_1} = \left(\frac{\partial a}{\partial s_1}\right)^2 \frac{\partial \mathbf{R}}{\partial a} \cdot \frac{\partial \mathbf{R}}{\partial a} = \frac{x_0'(a)^2 + y_0'(a)^2}{x_0'(a)^2 + y_0'(a)^2} = 1, \tag{54}$$

$$G = \frac{\partial \mathbf{R}}{\partial s_2}\cdot\frac{\partial \mathbf{R}}{\partial s_2} = \frac{\partial \mathbf{R}}{\partial z}\cdot\frac{\partial \mathbf{R}}{\partial z} = 1, \tag{55}$$

$$L = \frac{\partial^2 \mathbf{R}}{\partial s_1^2}\cdot\mathbf{n} = \frac{x_0'(a)y_0''(a) - x_0''(a)y_0'(a)}{[x_0'(a)^2 + y_0'(a)^2]^{3/2}},$$
$$N = \frac{\partial^2 \mathbf{R}}{\partial z^2}\cdot\mathbf{n} = 0. \tag{56}$$

The substrate and normal vectors are:

$$\mathbf{e}_1 = \frac{1}{E^{1/2}}\frac{\partial \mathbf{R}}{\partial s_1} = \frac{(x_0'(a), y_0'(a), 0)}{\sqrt{x_0'(a)^2 + y_0'(a)^2}},$$
$$\mathbf{e}_2 = \frac{1}{G^{1/2}}\frac{\partial \mathbf{R}}{\partial z} = (0,0,1),$$
$$\mathbf{n} = \mathbf{e}_1 \times \mathbf{e}_2 = \frac{(-y_0'(a), x_0'(a), 0)}{\sqrt{x_0'(a)^2 + y_0'(a)^2}}.$$

The curvature terms are:

$$\kappa_1 = \frac{L}{E} = \frac{x_0'(a)y_0''(a) - x_0''(a)y_0'(a)}{[x_0'(a)^2 + y_0'(a)^2]^{3/2}}, \quad \kappa_2 = \frac{N}{G} = 0, \tag{57}$$

and the pressure may be written:

$$p = p_0 - \sigma\left[\kappa_1 + \kappa_1^2(b+h) + \frac{\partial^2}{\partial s_1^2}(b+h) + \frac{\partial^2}{\partial z^2}(b+h)\right]. \tag{58}$$

The operator and fluxes in Eq. (17) are the same as in the flat surface case with x replaced by s_1.

5. Results

The coupled ice growth and water flow model is now applied to the three practical substrate shapes studied in the 'Standard Form' section, namely flat, aerofoil and cylindrical. The flat surface model involves flow driven by a constant shear stress and gravity and a Gaussian form for the incoming liquid. This might not be physically realistic but the behaviour of ice and water is then relatively easy to understand and check and the features observed are retrieved in the aerofoil and cylindrical cases. Note that in all the following examples, the mass loss or gain due to evaporation and sublimation is neglected.

5.1. Numerical method

Numerical solution for combined ice growth and water flow was examined extensively in [16]. Only the main points are recalled here.

A typical finite difference scheme in conservative form for Eq. (17) is

$$h_{i,j}^{k+1} = h_{i,j}^{k} - \frac{\Delta t}{(EG)^{1/2}}\left(G^{1/2}\frac{Q_{i+1/2,j}^{s_1} - Q_{i-1/2,j}^{s_1}}{\Delta s_1} + E^{1/2}\frac{Q_{i,j+1/2}^{s_2} - Q_{i,j-1/2}^{s_2}}{\Delta s_2}Q^{s_2}\right) + \frac{\rho_A}{\rho_w}\beta \mid \mathbf{W}\cdot\mathbf{n}\mid_{i,j}\Delta t - \frac{1}{\rho_w}\dot{m}_e\Big|_{i,j}\Delta t - \frac{\rho_i}{\rho_w}\frac{\partial b}{\partial t}\Big|_{i,j}^{k}\Delta t, \tag{59}$$

where $Q_{i+1/2,j}^{s_1}$ and $Q_{i,j+1/2}^{s_2}$ are the fluxes in the centre of the boundaries between cells $(i,j) - (i+1,j)$ and $(i,j) - (i,j+1)$ respectively. A semi implicit method is used to evaluate the fluxes. The derivatives $\partial h/\partial s_1$, $\partial^3 h/\partial s_1^3$, $\partial h/\partial s_2$ are $\partial^3 h/\partial s_2^3$ are calculated with a Crank–Nicholson scheme. All other terms are calculated explicitly. The corresponding parts of the flux are discretised with a Roe and Sweby scheme using a Superbee limiter to prevent shocks from developing [42]. For further details, see [16].

The ice growth rate is defined by Eqs. (33) and (39) respectively. Typical finite difference schemes for these equations are:

$$b_{i,j}^{k+1} = b_{i,j}^{k} + \frac{\Delta t}{\rho_i}(\beta \mid \mathbf{W}\cdot\mathbf{n} \mid \rho_A - \dot{m}_s), \tag{60}$$

$$b_{i,j}^{k+1} = b_{i,j}^{k} + \frac{k_i \Delta t}{\rho_i L_f}\frac{T_f - T_s}{b_{i,j}^{k}} - \frac{k_w \Delta t}{\rho_i L_f}\frac{E_g - F_g T_f}{1 + F_g h_{i,j}^{k}}. \tag{61}$$

In order to determine which model, rime or glaze, is appropriate at a given point, the following method is applied, see Fig. 3.

(1) The water fluxes are calculated at the boundary of each of the cells.
(2) The water and ice heights are calculated with the wet surface Equations (59) and (61). This requires that $b_i^k \neq 0$. For this reason, a precursor ice film, b_{prec}, is specified.
(3) If the new calculated water height is greater than the precursor film h_{prec}, the glaze ice model is selected.
(4) If the new calculated water height is smaller than the precursor film h_{prec}, this means there is no water on top of the ice. The calculated value for the water height is replaced by the precursor film height and a new ice height is calculated using Eq. (60). To conserve mass, a correction flux is applied at the rime/glaze interface.

This algorithm ensures continuity and physically sensible results for the water height as well as mass conservation.

5.2. Flat surface

The algorithm is first tested on an inclined flat surface. This example is run with shear stress acting along

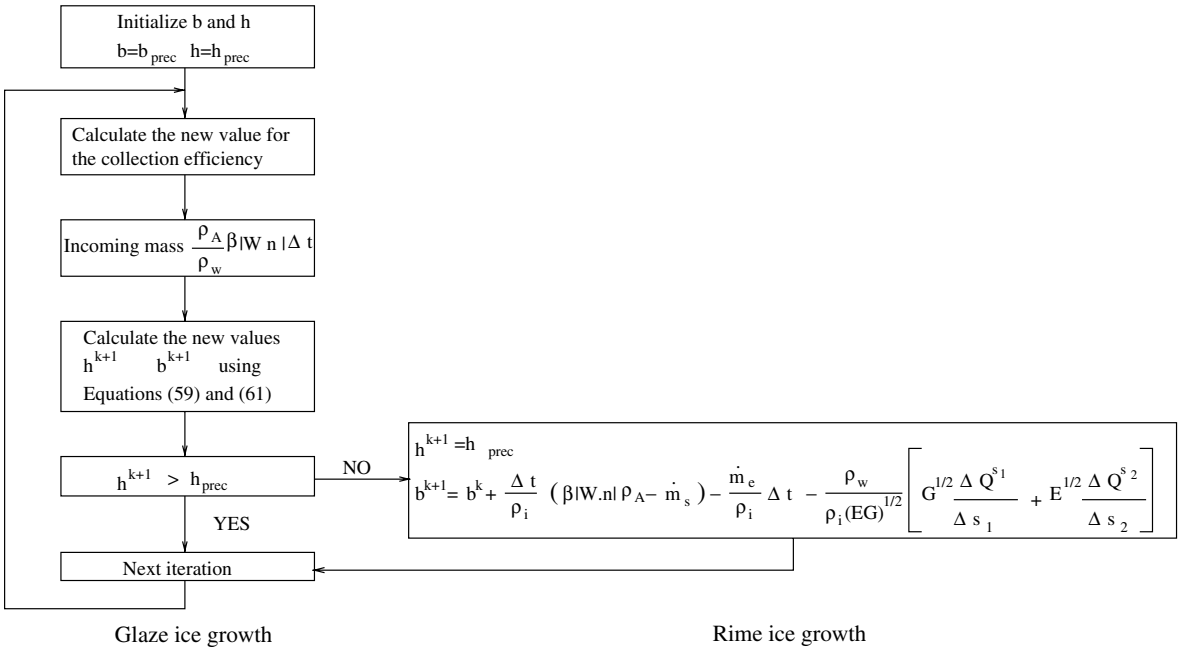

Fig. 3. Ice growth algorithm.

the diagonal from bottom left to top right, $A_1 = A_2 = 0.5\,\mathrm{Pa}$, gravity acts in the opposite direction $(G_1, G_2) = (4410, 4410)$, the free stream velocity is $W = 90\,\mathrm{m\,s^{-1}}$. The temperature is close to freezing, the ambient temperature is chosen as $T_a = 272\,\mathrm{K}$, droplets are at the same temperature $T_d = 272\,\mathrm{K}$ and the substrate is slightly colder, $T_s = 271\,\mathrm{K}$. These relatively high temperatures allow a significant water layer to develop and so allows a study of its behaviour. These values combined with the data in Table 2 lead to

$$E_g = 4.20 \times 10^5 + 2 \times 10^3 \beta \mid \mathbf{W} \cdot \mathbf{n} \mid, \tag{62}$$

$$F_g = 1.54 \times 10^3 + 7.4 \beta \mid \mathbf{W} \cdot \mathbf{n} \mid, \tag{63}$$

$$\beta \mid \mathbf{W} \cdot \mathbf{n} \mid = 45 \exp[-460(s_1^2 + s_2^2)]. \tag{64}$$

Results are computed for 70 s with $\Delta t = 5 \times 10^{-3}\,\mathrm{s}$ and $\Delta s_1 = \Delta s_2 = 0.0015\,\mathrm{m}$. The corresponding ice and water shapes may be seen in Figs. 4 and 5.

The accretion shown in Fig. 4 shows typical features of an accreting ice shape. A Gaussian region is in the centre of the accretion, corresponding to the incoming fluid. If all the impinging fluid were to freeze instantaneously when reaching the solid substrate, the ice accretion would have a Gaussian profile with a maximum height $b \approx 3.5\,\mathrm{mm}$. The present shape culminates at $b \approx 1.45\,\mathrm{mm}$: the difference is due to significant water flow, which is shown in Fig. 5. The ice layer extends on both sides of the central accretion following the water

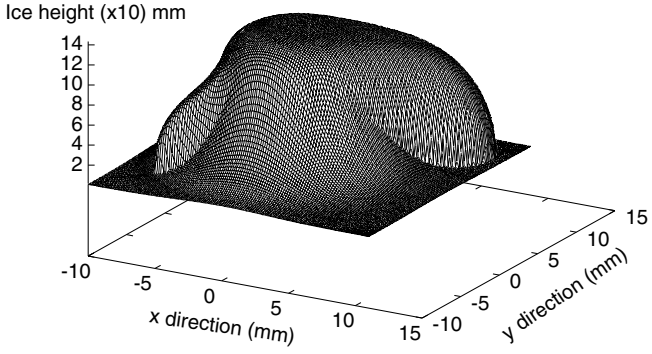

Fig. 4. Ice layer for a flat inclined surface.

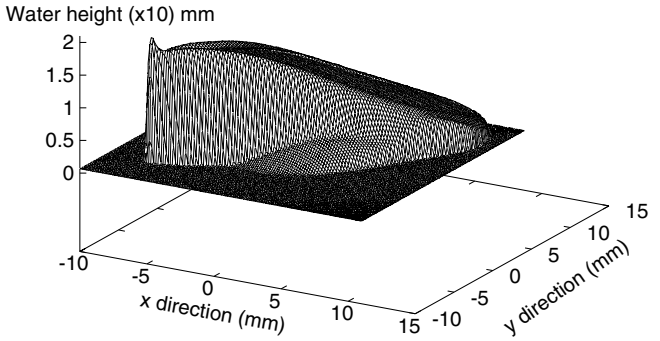

Fig. 5. Water layer for a flat inclined surface.

flow. The wide parabolic profile on the right of the layer is due to shear driven flow. The thin hump on the left is due to gravity. These two features are characteristic for an ice growth coupled with water flow and will be retrieved in the other examples. Fig. 5 shows the corresponding water film. The sharp peak on the left is known as a capillary ridge and is typical of such flows. In fact, in general, the flow to the right would normally show a similar ridge but it is suppressed by the ice accretion. Further details on accretion on a flat inclined plane may be found in [16,19,41].

5.3. Two-dimensional cylinder

In this application, ice accretion is studied on the external face of a cylinder of radius $R = 5\,\mathrm{cm}$. The problem configuration is shown in Fig. 6. The cylinder is placed in an ambient temperature $T_a = 271\,\mathrm{K}$, subject to freezing rain falling vertically. The temperature of the rain droplets is $T_d = 271\,\mathrm{K}$. Their velocity when they hit the cylinder is $W = 5\,\mathrm{m\,s^{-1}}$. This value may occur in rain storms and will therefore be used in the following [48]. The liquid water content $\rho_a = 0.001\,\mathrm{kg\,m^{-3}}$ leads to a rain intensity of $18\,\mathrm{mm\,h^{-1}}$. Note this is relatively high rate, but as such it leads to significant water flow

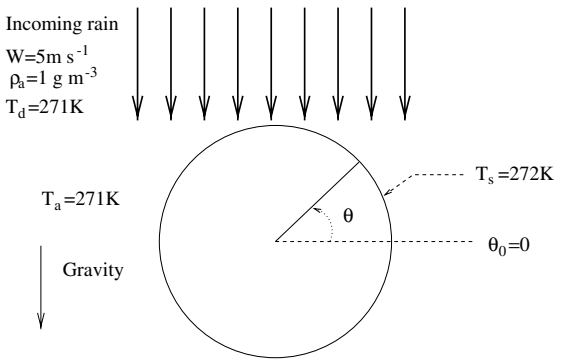

Fig. 6. Typical geometry parameters on a circular cylinder.

which is a much more rigorous test of the model than if there is only slight water motion.

No air flow around the cylinder will be considered, the droplets and the water layer are only subject to gravity that acts vertically from top to bottom, in the direction $\theta = -90°$. The temperature around the cylinder and the heat transfer coefficient may therefore be taken as constant $T = 271\,\mathrm{K}$, $H = 50\,\mathrm{W\,m^{-2}\,K^{-1}}$. Finally, the temperature at the surface of the cylinder, $T_s = 272\,\mathrm{K}$, is chosen slightly higher than T_a to permit a model for internal heating, see [49] and references therein. With these values, the impinging mass rate on the clean surface is

$$\beta \mid \mathbf{W}\cdot\mathbf{n} \mid = \begin{cases} -5\cos\theta & \pi/2 \leqslant \theta \leqslant 3\pi/2, \\ 0 & \text{otherwise} \end{cases} \tag{65}$$

and this is updated at each time step of the computation. The energy terms are

$$E_g = 4.15\times 10^4 + 2\times 10^3 \beta \mid \mathbf{W}\cdot\mathbf{n} \mid, \tag{66}$$

$$F_g = 1.54\times 10^3 + 7.4\beta \mid \mathbf{W}\cdot\mathbf{n} \mid . \tag{67}$$

Figs. 7 and 8 show the evolution of the ice layer for an hour in the freezing rain conditions described above. Results are computed for $\Delta\theta = 0.5°$ and $\Delta t = 0.002\,\mathrm{s}$. As the surface temperature is below freezing, at the start of the accretion, all impinging droplets first turn into ice when they reach the surface and the ice layer follows the shape of the collection efficiency so there is initially no ice below $y = 0$. The water layer starts developing from the top of the cylinder where $\theta = 90°$, shortly before $t = 5\,\mathrm{min}$. Soon the water reaches the extent of the initial iced region and flows into the sheltered area, below $y = 0$, the ice shape then starts to extend around the cylinder.

Fig. 7a shows the ice shape after 15 min, already there is ice well below $y = 0$. The ice evolves progressively from the initial shape inherited from the collection efficiency to a less smooth profile. The thickness does not vary significantly on the upper part of the cylinder,

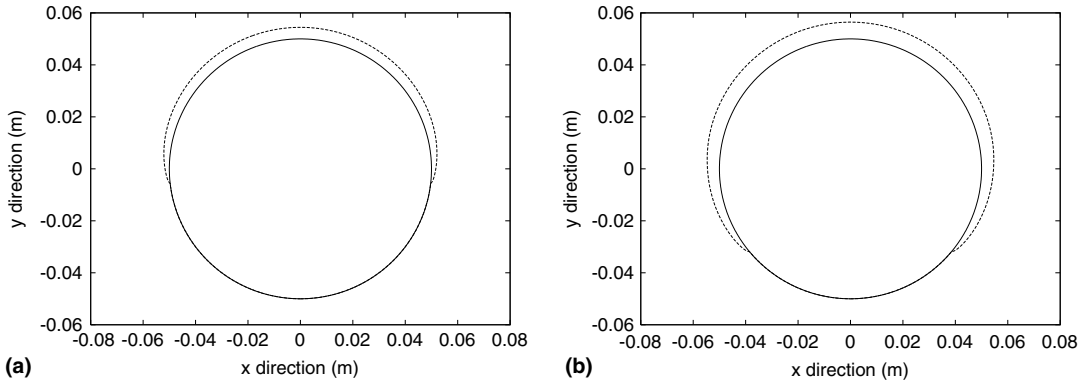

Fig. 7. Ice layers on a cylinder at $t = 15$ min (a) and $t = 30$ min (b).

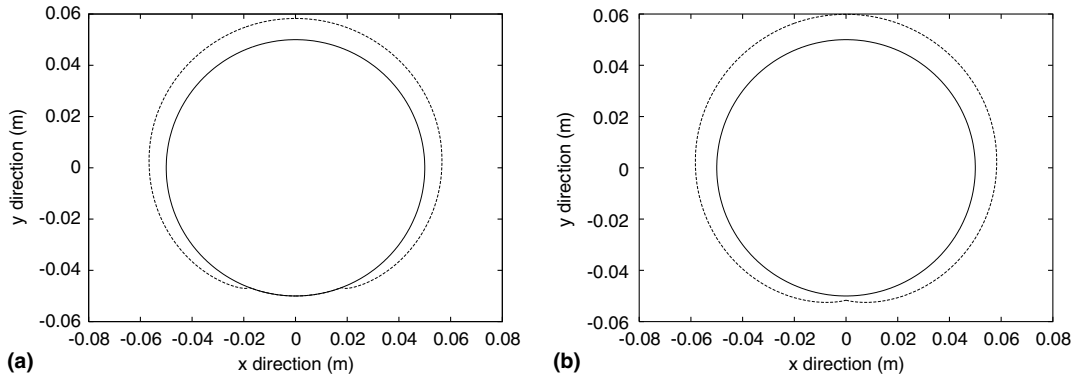

Fig. 8. Ice layers on a cylinder at $t = 45$ min (a) and $t = 60$ min (b).

$90° < \theta < 270°$. On the lower part, the thickness decreases smoothly as y decreases with the characteristic parabolic profile. The water layer reaches the bottom of the cylinder, $\theta = 0°$ shortly before $t = 60$ min as shown in Fig. 8b. Subsequently, the ice layer grows quickly and soon, the ice thickness is almost constant all around the cylinder. However, the model reaches its limit here. Shortly after this, the calculated results are not physically realistic. In reality, all the impinging water may now flow quickly towards the bottom of the cylinder to form droplets. The thin film flow may not be applied any more. It should be replaced with a model where droplets form and fall off, also, icicles would start growing [3].

Szilder et al. [51] publish numerical results for ice accretion on a cable, however their ice shape depends on a specified parameter S, which determines how far water will flow, and the final rainfall amount. In the current model, the ice shape depends on a water flow which is determined by the underlying physics. Further, whilst the final rainfall amount will determine the weight of ice, it is really the rainfall distribution that plays a significant role in determining the shape (for example, more rain will hit the top of the cable where $\theta = \pi/2$, than the sides, $\theta = 0, \pi$). The current method would certainly produce a similar result to one of those shown in their work but this would not validate either method.

5.4. Two-dimensional aerofoil

Ice accretion on an aerofoil is now briefly studied. Results are calculated for a NACA0012 aerofoil at zero angle of attack. The configuration for this case is shown in Fig. 9. The wing is placed in a mild freezing environment, $T_a = 270$ K. Supercooled droplets at the same temperature, $T_d = 270$ K, are carried from left to right by the air, which has a free stream velocity $W = 50\,\mathrm{m\,s^{-1}}$, and hit the forward facing part of the wing. The liquid water content is taken as $\rho_a = 0.001\,\mathrm{kg\,m^{-3}}$. The wing temperature is maintained at $T_s = 269$ K. This value is different from the ambient temperature to demonstrate the capability of including internal heating or cooling. The shape

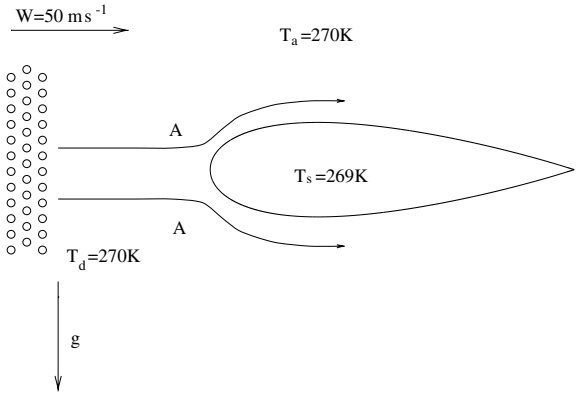

Fig. 9. Initial problem configuration for aerofoil icing.

of the ice-clear aerofoil may be described using Bézier splines of order 8 [46]. The upper part of the aerofoil is defined by

$$x(a) = \sum_{i=0}^{8} \mathscr{C}_8^i x_i a^i (1-a)^{(8-i)}, \tag{68}$$

$$y(a) = \sum_{i=0}^{8} \mathscr{C}_8^i y_i a^i (1-a)^{(8-i)}, \tag{69}$$

where $a \in [0,1]$ and the points (x_i, y_i) are given in Table 3. The lower part may be obtained by symmetry.

The pressure p_0 and shear stress, A_1 are computed using the CFD package Fluent. The collection efficiency, β, is defined as the ratio between the surface a given mass of water passes through in the free stream and the surface it covers on the substrate [1]. This parameter is evaluated from droplet trajectories, also computed in Fluent. The heat transfer coefficient is evaluated using the formula [1,47]:

$$H = \frac{0.296 k_{\text{air}}}{\sqrt{\mu_{\text{air}}/\rho_{\text{air}}}} \sqrt{\frac{V^{2.87}}{\int_0^s V^{1.87}\,\mathrm{d}r}}, \tag{70}$$

Table 3
Interpolation points for the Bézier spline representation of a NACA0012

	x_i	y_i
0	0.0	0.0
1	0.0	0.18556
2	0.03571	0.34863
3	0.10714	0.48919
4	0.21429	0.58214
5	0.35714	0.55724
6	0.53571	0.44992
7	0.75	0.30281
8	1.0	0.0105

where k_{air}, $\mu_{\text{air}}\rho_{\text{air}}$ are the conductivity, dynamic viscosity and density of the air respectively and V is the velocity at edge of the boundary layer.

The ice layer for the first 15 min of the accretion may be seen in Figs. 10 and 11. These results are computed with $\Delta s = 0.1$ mm and $\Delta t = 5 \times 10^{-4}$ s. The impinging water impacts to the left of $x \approx -0.105$ although the majority hits close to the leading edge. Since the substrate temperature is below freezing, rime ice grows initially. Water appears shortly after $t = 90$ s. The ice shape at $t = 3$ min is shown on Fig. 10a. Already the effect of the water flow may be seen. The ice does not project as far forward as it would in the rime case. The top has been flattened out as the water spreads. The extent of the spread may be inferred from the kink in the ice shape at $x \approx -0.145$. As time continues the ice shape grows and the water flows further around the aerofoil.

Fig. 10b shows the ice shape after 6 min. The water has now reached $x \approx -0.133$. The shapes after 9 and 15 min are shown in Fig. 11. A noticeable feature of both these diagrams is the dip that has formed at the leading edge. This is due to a sharp drop observed in the heat transfer coefficient at this location. This variation becomes more important with time.

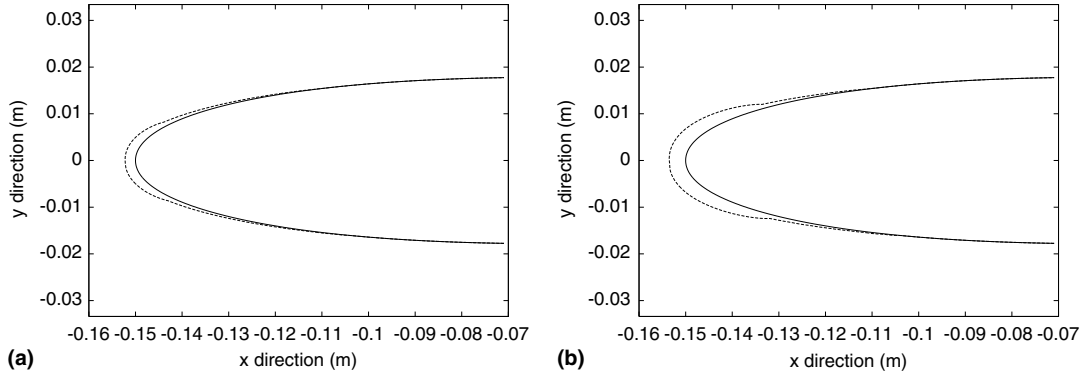

Fig. 10. Ice layers on a NACA0012 at $t = 3$ min (a) and $t = 6$ min (b).

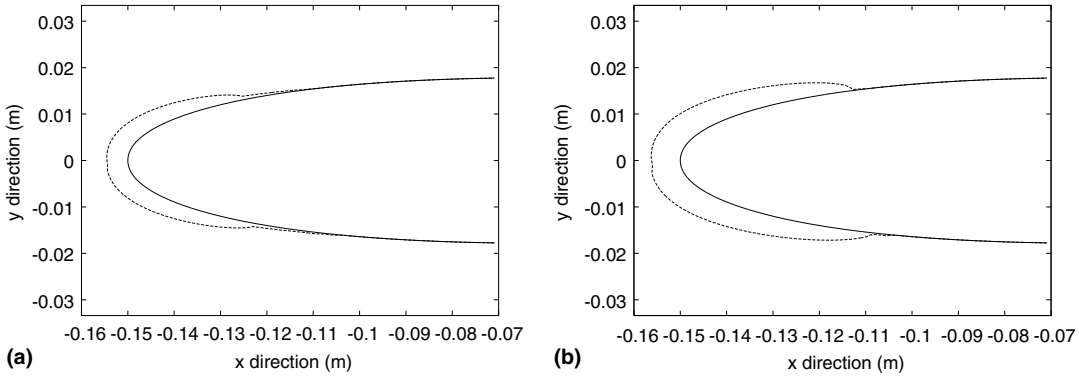

Fig. 11. Ice layers on a NACA0012 at $t = 9$ min (a) and $t = 15$ min (b).

The water layer for times 3 and 15 min is shown in Fig. 12. Since the water layer is so thin it is drawn on an unfolded aerofoil to clarify the shape. Negative and positive values of the s coordinate correspond to the lower and upper parts of the aerofoil respectively, $s = 0$ denotes the leading edge position. The water extension is limited to $s \in [-1.1{:}1.05]$ cm at $t = 3$ min with the lower part slightly more extended due to gravity. The region covered with fluid increases steadily to reach $[-4.6{:}4.2]$ cm at $t = 15$ min. The shape of the water layer remains similar throughout the simulation. A high peak forms around $s = 0$. At this location, the shear stress is very small and the water level is too low for the fluid to be moved significantly by gravity, although its effects are maximum there. Fluid impacting in this region moves away very slowly. Its speed increases as it moves out to regions with a higher shear stress.

In Fig. 11, the shape of the ice layer is closely related to the evolution of the water layer. When covered with fluid, the ice loses the form of the collection efficiency and takes a more rounded shape. At the top, the accretion rate reduces progressively as the ice layer becomes thicker, allowing more water to be pushed away from the leading edge. At $t \approx 15$ min, the extension of the catch is reached and from this moment, ice is growing on zones with no impinging water droplets. Further evolution of the ice layer may easily be predicted: the shape will remain very similar with the accretion rate slowing down progressively at the leading edge and the layer continuing to extend.

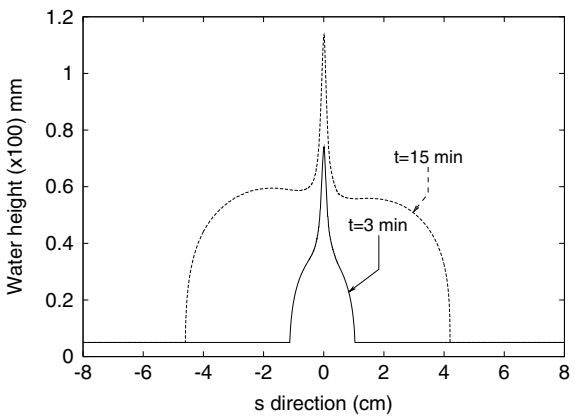

Fig. 12. Water layer at $t = 3$ min (a) and $t = 15$ min (b).

A significant feature of these results is that the runback film does not extend a long way past the impingement zone. Codes that do not employ a lubrication model typically show an extended runback zone, in poor agreement with experimental results. Makkonen et al. [9] observe 'relatively poor agreement' between their TURBICE model and experiment during wet growth. However, they also run LEWICE which has significantly worse results, the predicted runback region extends beyond the edge of the figure, the experimental result is confined near the leading edge. They also mention similar problems occur with the THERMICE model of Tranh et al. [52]. The current model is employed in a commercial icing code, ICECREMO. In a discussion of the validation of this code Dr. Bartlett of Rolls-Royce summarised by saying "*In general the model predictions agree well with experimental data. The ice microstructure studies indicated an initial zone of rime ice, with the fine grains becoming coarse as water developed at the accretion front. This behaviour is predicted by the model, with the ice thickness at which the water is first predicted correlating closely with the thickness of the fine grain zone... With small ice accretions, relative to the size of the geometry considered, there is excellent agreement between the predicted and measured ice thickness. The extent of the ice also gives reasonable comparison*", see [22].

6. Conclusion

The work described in this paper provides a model for ice accretion and water flow based on well estab-

lished theories. As such, provided the model restrictions (such as thin water layer) are not broken it should provide accurate results. Obviously there are limitations to such a model. The input parameters can be very difficult to obtain accurately and this subject forms a whole new but complementary field of research. The initial rime ice may form a very rough surface, which will have a significant effect on any water flow.

In practical terms it is a difficult task to incorporate a complex numerical code to describe ice accretion and water flow into already complicated icing codes. However, a testament to this type of model is that an earlier, simpler version is currently employed in a commercial aircraft icing code, ICECREMO.

It has been shown how the model may be applied to standard substrate shapes and two examples relating to inflight and atmospheric icing were detailed. However, the model is quite general and can be applied to any substrate shape. There is also much potential for improvement. For example a more intimate coupling between the air and water flow. Substrate heating could be incorporated to model anti-icing systems. This is currently being investigated.

Acknowledgment

The authors acknowledge the support of this work by the National Research Foundation of South Africa, under grant number 2053289, and the Claude Harris Foundation.

References

[1] R.W. Gent, N.P. Dart, J.T. Cansdale, Aircraft icing, Philos. Trans. R. Soc. Lond. A 358 (1776) (2000) 2873–2911.
[2] S.K. Thomas, R.P. Cassoni, C.D. MacArthur, Aircraft anti-icing and de-icing techniques and modelling, J. Aircraft 33 (5) (1996) 841–854.
[3] L. Makkonen, Models for the growth of rime, glaze icicles and wet snow on structures, Philos. Trans. R. Soc. Lond. A 358 (2000) 2913–2939.
[4] E.P. Lozowski, K. Szilder, L. Makkonen, Computer simulation of marine ice accretion, Philos. Trans. R. Soc. Lond. A (358) (2000) 2811.
[5] G.I. Poots, Ice and Snow Accretion on Structures, Research Studies Press, 1996.
[6] M. Farzaneh, Ice accretions on high-voltage conductors and insulators and related phenomena, Philos. Trans. R. Soc. Lond. A 358 (2000) 2971.
[7] S. Elliot, G. Warwick, Flying on thin ice, Flight Int. 29 (April–May) (1992).
[8] D. Hughes, Safety group highlights CFIT risk for regionals, Aviation Week Space Technol. 140 (19) (1994) 46.
[9] L. Makkonen, T. Laakso, M. Marjaniemi, K.J. Finstad, Modelling and prevention of ice accretion on wind turbines, Wind Eng. 25 (1) (2001) 3–21.
[10] Y. Bourgault, H. Beaugendre, W.G. Habashi, Development of a shallow-water icing model in FENSAP-ICE, J. Aircraft 37 (4) (2000) 640–646.
[11] W.B. Wright, R.W. Gent, D. Guffond, DRA/NASA/ONERA collaboration on icing research part II—Prediction of airfoil ice accretion, NASA CR-202349, May 1997.
[12] B.L. Messinger, Equilibrium temperature of an unheated icing surface as a function of air speed, J. Aero. Sci. (January) (1953) 29–42.
[13] T.G. Myers, An extension to the Messinger model for aircraft icing, AIAA J. 39 (2) (2001) 211–218.
[14] T.G. Myers, D.W. Hammond, Ice and water film growth from incoming supercooled droplets, Int. J. Heat Mass Transfer 42 (1999) 2233–2242.
[15] H. Ockendon, J.R. Ockendon, Viscous Flow, Cambridge Texts in Applied Mathematics, Cambridge University Press, 1995.
[16] T.G. Myers, J.P.F. Charpin, S.J. Chapman, The flow and solidification of a thin fluid film on an arbitrary three-dimensional surface, Phys. Fluids 14 (8) (2002) 2788–2803.
[17] J.A. Moriarty, L.W. Schwartz, E.O. Tuck, Unsteady spreading of thin liquid films with small surface tension, Phys. Fluids A 3 (5) (1991) 733–742.
[18] T.G. Myers, Thin films with high surface tension, SIAM Rev. 40 (3) (1998) 441–462.
[19] T.G. Myers, J.P.F. Charpin, C.P. Thompson, Slowly accreting glaze ice due to supercooled water impacting on a cold surface, Phys. Fluids 14 (1) (2002) 240–256.
[20] L. Makkonen, Analysis of rotating multicylinder data in measuring cloud-droplet size and liquid water-content, J. Atmos. Oceanic Tech. 9 (3) (1992) 258–263, June.
[21] A. Defina, Two-dimensional shallow flow equations for partially dry areas, Water Resour. Res. 36 (11) (2000) 3251–3264.
[22] P. Bartlett, Development of a new model of ice accretion on aircraft, In: Proceedings of 9th International Workshop on Atmospheric Icing on Structures, Chester, UK June, 2000.
[23] L. Makkonen, M. Auttti, The effects of icing on wind turbines, in: Wind Energy—Technology and Implementation, Elsevier Science Publishing, 1991.
[24] A.C. Fowler, Mathematical Models in the Applied Sciences, Cambridge University Press, 1997.
[25] I.A. Frigaard, Solidification of spray formed billets, J. Eng. Math. 31 (1997) 411–437.
[26] E. Gutierrez-Miravete, E.J. Lavernia, G.M. Trapaga, J. Szekely, N.J. Grant, Mathematical model of the spray deposition process, Metall. Trans. A 20A (1989) 71–85.
[27] J.R. Lister, The solidification of buoyancy-driven flow in a flexible-walled channel. Part1. Constant-volume release, J. Fluid Mech. 272 (1994) 21–44.
[28] A.D.D. Craik, Wind generated waves in thin liquid films, J. Fluid Mech. 26 (2) (1966) 369–392.
[29] A.C. King, E.O. Tuck, J.M. Vanden Broeck, Air-blown waves on thin viscous sheets, Phys. Fluids A 5 (4) (1993) 973–978.

[30] J.-C. Tsao, A.P. Rothmayer, A.I. Ruban, Stability of air flow past thin liquid films on airfoils, Comput. Fluids 26 (5) (1997) 427–452.
[31] C.-S. Yih, Wave formation on a liquid layer for de-icing airplane wings, J. Fluid Mech. 212 (1990) 41–53.
[32] S. Middleman, The effect of induced air flow on the spin coating of viscous liquids, J. Appl. Phys. 62 (6) (1987) 2530–2532.
[33] D.E. Weidner, L.W. Schwartz, M.H. Eres, Simulation of coating layer evolution and drop formation on horizontal cylinders, J. Colloid Interface Sci. 187 (1997) 243–258.
[34] P.D. Howell, Surface-tension-driven flow on a moving curved surface, J. Eng. Math. 45 (3–4) (2003) 283–308.
[35] D.E. Bourne, P.C. Kendall, Vector Analysis and Cartesian Tensors, third ed., Chapman Hall, 1992.
[36] L. Makkonen, A model of icicle growth, J. Glaciol. 34 (1988) 64–70.
[37] K. Arnold, G. Tetzlaff, A. Raabe, Modelling of ice accretion on a non-rotating cylinder, Meteorol. Zeitschrift 6 (3) (1997) 120.
[38] A.L. Bertozzi, The mathematics of moving contact lines, Notices AMS (June/July) (1998) 689–697.
[39] E.B. Dussan V, On the spreading of liquids on solid surfaces: static and dynamic contact lines, Ann. Rev. Fluid Mech. 11 (1979) 371–400.
[40] K. Stoev, E. Ramè, T. Leonhardt, S. Garoff, The effects of thin films on the hydrodynamics near moving contact lines, Phys. Fluids 10 (8) (1998) 1793–1803.
[41] J.P.F. Charpin, Water flow on accreting ice surfaces, PhD thesis, Cranfield University, November, 2002.
[42] H.Q. Yang, J. Przekwas, A comparative study of advanced shock-capturing schemes applied to Burgers equation, J. Comput. Phys. 102 (1) (1992) 139–159.
[46] W. Boehm, Bézier presentation of airfoils, Comput. Aided Geom. Des. 4 (1) (1987) 17–22.
[47] G. Mingione, V. Brandi, Ice accretion prediction on multielement airfoils, J. Aircraft 35 (2) (1998) 240–246.
[48] H.R. Pruppacher, Microstructure of atmospheric clouds and precipitation, in: P.V. Hobbs, A. Deepak (Eds.), Clouds, Their Formation, Optical Properties and Effects, Academic Press, 1981.
[49] J.L. Laforte, M.A. Allaire, J. Laflamme, State of the art on power line de-icing, Atmos. Res. 46 (1-2) (1998) 143–158.
[51] K. Szilder, E.P. Lozowski, G. Reuter, A study of ice accretion shape on cables under freezing rain conditions, ASME J. Offshore Mech. Arctic Eng. 124 (3) (2002) 162–168.
[52] P. Tranh, M.T. Brahimi, I. Paraschivoiu, A. Pueyo, F. Tezok, Ice accretion on aircraft wings with thermodynamic effects, J. Aircraft 32 (2) (1994) 444–446.